Int. J. Heat Mass Transfer. Vol. 30, No. 7, pp. 1237–1246, 1987
Printed in Great Britain

0017–9310/87 $3.00 + 0.00
Pergamon Journals Ltd.

Relation between the points of flow reattachment and maximum heat transfer for regions of flow separation

E. M. SPARROW, S. S. KANG and W. CHUCK
Department of Mechanical Engineering, University of Minnesota, Minneapolis, MN 55455, U.S.A.

(*Received* 26 *August* 1986 *and in final form* 3 *November* 1986)

Abstract—The streamwise distribution of the Nusselt number within and just downstream of a region of flow separation displays a maximum whose location, relative to the point of reattachment of the flow, was investigated here. Wind tunnel experiments were performed in which a circular cylinder was oriented longitudinal to a uniform freestream. Due to flow separation at the outer rim of the forward face of the cylinder, the upstream portion of the cylindrical surface was washed by a zone of recirculating fluid. Three configurations of the longitudinal cylinder were investigated: one with a solid, blunt forward face, a second with a hollow bore open at both its upstream and downstream ends, and a third in which the hollow bore was closed at its downstream end. The blunt-face case was also solved numerically. Additional numerical solutions were carried out for the contrastingly different case of an abrupt enlargement in a parallel-plate channel. Both the experimental and numerical results provided conclusive evidence that the commonly assumed equality of the points of flow reattachment and maximum heat transfer coefficient was, at best, a special case. For most of the cases investigated here, the heat transfer maximum occurred upstream of the reattachment point. Factors influencing the relative positions of the maximum and the reattachment were identified.

INTRODUCTION

FLUID flows which are unable to follow a rapid change in the contour of the surface which bounds the flow are said to separate from the surface. For instance, separated flows occur in the presence of sudden enlargements and contractions, partial blockages, and sharp turns. Depending on the downstream configuration of the bounding surface, the separated flow will reattach and then undergo a redevelopment. The region situated between the points of separation and reattachment (sometimes called the separation bubble) contains a recirculating flow.

The streamwise distribution of the heat transfer coefficient within and downstream of the separated region is typically characterized by an initial increase which leads to the attainment of a maximum and a subsequent decrease. At sufficiently great downstream distances, the distribution takes on the trendwise characteristics that correspond to the redeveloped flow.

In the very considerable literature dealing with heat transfer in separated flows, it is generally assumed that the aforementioned heat transfer maximum occurs at a streamwise location x_{max} that coincides with the location x_r at which the flow reattaches (both x_{max} and x_r are measured from the point of separation). There is, however, considerable evidence that the assumed equality of x_{max} and x_r is by no means universal. The inequality of x_{max} and x_r has been noted by various authors, as will be documented shortly, but only as a minor side issue within the framework of a larger investigation. In contrast, the present paper is totally focused on the relationship between x_{max} and x_r.

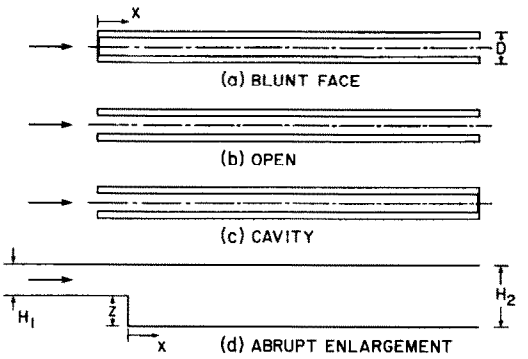

FIG. 1. Investigated fluid flow configurations.

The fluid flow configurations to be examined here are pictured schematically in Fig. 1. Figures 1(a)–(c) depict three versions of a circular cylinder whose axis is aligned longitudinal to an extensive freestream flow. In the first of these, to be denoted as the blunt-face case, the upstream face of the cylinder is a solid surface. In the case shown in Fig. 1(b), the bore of the cylinder is open at both its upstream and downstream ends, so that the oncoming stream may, in part, flow through the bore as well as pass over the external surface. In the third case, the downstream end of the bore is closed, forming a cavity open at its upstream end. If fluid from the oncoming flow penetrates the open end of the cavity, an equal amount must exit the same end in order to satisfy mass conservation.

NOMENCLATURE

D	outer diameter of cylinder	T_1	pre-enlargement fluid temperature
H_1	pre-enlargement height of channel	T_∞	freestream temperature
H_2	post-enlargement height of channel	U_∞	freestream velocity
h	local heat transfer coefficient, equations (1) and (5)	u	streamwise velocity component
		$\bar{u}_1$	pre-enlargement mean velocity
h_1	local heat transfer coefficient, equation (6)	x	axial coordinate
		x_{max}	location of maximum Nusselt number
k	thermal conductivity	x_r	location of flow reattachment
q	local convective heat flux	y	transverse coordinate
Pr	Prandtl number	z	step height.
R	outer radius of cylinder		
Re	Reynolds number, equations (3) and (7)	Greek symbols	
r	radial coordinate	ε	emissivity
T_b	bulk temperature	ν	kinematic viscosity
T_w	wall temperature	σ	Stefan–Boltzmann constant.

The oncoming flow separates at the outer rim of the upstream face of the cylinder and reattaches downstream on the exterior surface. In the situations to be investigated here, the exterior surface was uniformly heated while the other surfaces were unheated.

Complementary heat transfer and fluid flow experiments were performed to determine x_{max} and x_r on the exterior surface of configurations (a)–(c). The experiments were carried out in air in a low-turbulence wind tunnel over the Reynolds number range from about 7500 to 47,500. Values of x_{max} were obtained by identifying the peak in the measured axial distributions of the local Nusselt number. The oil–lampblack flow visualization technique was used for the determination of x_r.

As a supplement to the experimental work, the blunt-face case was singled out for numerical study. A laminar model was adopted, and a finite-difference solution was carried out. From the solution, x_{max} was obtained from the computed axial distribution of the local Nusselt number, in the same manner as in the experiments, while x_r was now determined by identifying the location at which a change of sign occurred in the axial distribution of the local wall shear stress.

To provide a broad perspective on the relationship between x_{max} and x_r, it was deemed appropriate to investigate another configuration, one which differs markedly from that of Figs. 1(a)–(c). To this end, consideration was given to an unsymmetric abrupt enlargement in a parallel-plate channel, as depicted in Fig. 1(d). The heating was also unsymmetric, being confined to the lower wall of the enlarged portion of the channel. A laminar model was also employed for this problem, and finite-difference solutions were carried out for step-height Reynolds numbers in the range from 100 to 300. The solutions yielded axial distributions of the local Nusselt number and the local wall shear stress, from which x_{max} and x_r were determined.

Attention will now be turned to the literature relevant to the relationship between x_{max} and x_r. For the blunt-face cylinder in longitudinal flow (Fig. 1(a)), the reattachment point x_r was measured by three different methods in ref. [1], and the average value, $x_r/D = 1.6$, was adopted. From the heat transfer measurements of ref. [2], it was reported that $x_{max}/D = 1.4$; however, careful inspection of Fig. 1 of ref. [2] indicates that $x_{max}/D = 1.3$ is probably a better representation of the data. The heat transfer characteristics of the blunt-face cylinder were investigated by a mass transfer analogy in refs. [3, 4], where it was tacitly assumed that $x_{max} = x_r$. There are no results in the literature for the open and cavity cases depicted in Figs. 1(b) and (c).

For the related case of the blunt-face plate in longitudinal flow, a group of companion papers [5–7] have yielded conflicting results. For the data presented in refs. [5, 6], $x_{max} < x_r$, whereas a comparison of refs. [6, 7] gave $x_{max} = x_r$. From the blunt-plate experiments of ref. [8], it was found that x_{max} exceeded x_r by 12–15%.

The configuration of Fig. 1(d) resembles the often-investigated backward-facing step but differs in that it pertains to an internal flow (hydrodynamically developed upstream of the step), whereas the prior work has dealt exclusively with external flows. For laminar flow [9], x_{max} was found to be substantially greater than x_r. In an early investigation of the turbulent case [10], it was concluded that $x_{max} = x_r$, where x_r was determined from velocity measurements. However, an examination of the dividing streamline (i.e. the streamline which bounds the separation bubble) suggests that reattachment occurs downstream of the Nusselt number maximum, i.e. $x_{max} < x_r$. The most recent study [11] of the turbulent case gave $x_{max} = 0.9\, x_r$.

To round out the literature survey, mention may be made of circular pipe results. For air flow in a pipe in which separation was created by a 70% enlargement of the diameter, x_{max} was about 35% greater than x_r [12]. In contrast, for separation caused by the presence

of an orifice plate in a pipe, x_{max} was reported to be 9–22% less than x_r [13].

The foregoing literature survey offers ample evidence refuting the commonly held assumption that $x_{max} = x_r$. However, the cited results do not fall into an orderly pattern.

EXPERIMENTAL APPARATUS

The longitudinal cylinder used in the experiments had an outer diameter of 4.862 cm and an overall streamwise length of 59.7 cm. The bore diameter was 2.761 cm, resulting in a bore length–diameter ratio of approximately 21.5.

The cylinder was an assembly of many components. The outer surface was a sheet of 0.00508-cm-thick stainless steel shim stock stretched tightly over a laminated phenolic tube (wall thickness = 0.170 cm) which had been pre-machined to ensure roundness. Ohmic dissipation due to current flow in the stainless steel sheet served as the heat source. Prior to the assembly, the exposed surface of the stainless steel sheet was painstakingly hand polished to a high luster to diminish the radiation heat transfer, and, after polishing, the emissivity was measured to be 0.10. The rear surface of the stainless steel sheet was instrumented with thermocouples and voltage taps made from Teflon-coated 0.00762-cm-diameter wire, chromel–constantan for the thermocouples and constantan for the taps. The thermocouples had been precalibrated prior to their installation.

Grooves had been machined in the phenolic backing tube to accommodate the wires, and to avoid extraneous heat conduction in the wires, the grooves were made circumferential. The thermocouples were positioned at 22 axial stations along a line parallel to the axis of the cylinder at locations which will be evident from the Nusselt number distributions to be presented later. At two axial stations, the third and the twentieth, four thermocouples were installed at 90° intervals around the circumference to enable the circumferential uniformity of the temperature to be verified.

The bore was formed by an aluminum tube having respective inner and outer diameters of 2.761 and 3.175 cm. The annular space between this aluminum tube and the aforementioned phenolic backing tube served as a passage through which the thermocouple and voltage tap wires were led to the downstream end of the apparatus. To guard against heat conduction through the annular space, it was filled with silica aerogel powder insulation whose thermal conductivity is 15% less than that of air.

For the open and cavity configurations, Figs. 1(b) and (c), the upstream face of the cylinder was formed by an annular aluminum disk whose bore had been shrunk-fit onto the inner aluminum tube. The outer rim of the disk was machined so as to mate without discontinuity with the phenolic backing tube and its overlayed stainless steel sheet. Electrical contact at the outer rim was achieved by means of a thin layer of silver paint. For the blunt-face configuration, Fig. 1(a), the bore was closed at its upstream end by an O-ring-equipped plexiglass disk. For all cases, painstaking machining operations were performed to ensure that the front face was a continuous, flat surface perpendicular to the axis of the cylinder. The plexiglass disk used to close the upstream end of the bore in the blunt-face case was used to close the downstream end of the bore in the cavity case.

The cylinder was suspended from the upper wall of the rectangular test section of a wind tunnel by vertical struts. The struts were situated at the downstream end of the cylinder, beyond the heated portion of the outer surface. As part of the support system, the outer surface of the cylinder beyond the heated section was formed by an aluminum sleeve. The outer diameters of the heated section and the support sleeve were identical, and their streamwise lengths were 49.3 and 10.4 cm.

The struts were thin stainless steel plates (0.19 cm thick) aligned parallel with the freestream, with rounded leading and trailing edges to further diminish the disturbance of the flow. In addition to their role as supports, the struts served to channel the thermocouple and voltage tap wires and the electric current, the latter with the aid of aluminum-filled grooves.

At their upper ends, the struts mated with a mounting plate built into the upper wall of the wind tunnel. The mounting plate allowed for two degrees of freedom in the positioning of the cylinder in order to obtain a circumferentially uniform temperature distribution. Adjustments were made until circumferential uniformity was indicated by the four thermocouples situated at measurement stations 3 and 20.

Electric current was provided by a d.c. supply stable to 0.01%. The series flow path of the current included the struts, the support sleeve, the aluminum inner tube, the aluminum front face disk, and the stainless steel sheet, but only in the latter did significant dissipation occur.

In addition to the thermocouples deployed along the rear surface of the stainless steel sheet, eight additional thermocouples were installed to measure temperatures on the front face disk, the inner tube, and at the downstream end of the insulation-filled annular space. The thus-measured temperatures were employed as boundary conditions for a finite-difference solution performed to determine the conduction heat losses from the rear surface of the stainless steel. The temperature of the freestream flow was measured by two thermocouples situated at the side of the cylinder.

The experiments were carried out in a wind tunnel having a 30.48×60.96 cm rectangular test section (height × width) which was 2.4 m long. The freestream velocity was measured upstream of the cylinder by an

impact tube and an associated wall static tap, with the pressure signals being read with a resolution of 10^{-3} Torr by a capacitance-type, solid-state pressure meter. At the operating conditions of the experiments, the freestream turbulence intensity was 0.4–0.5%. An equilibration period of $1\frac{1}{2}$ h was allowed before heat transfer data were collected for a given data run. Further details of the apparatus and the experimental techniques are available in a thesis [14] from which this paper is drawn.

FLOW VISUALIZATION

The axial station at which the separated flow reattached to the outer surface of the cylinder was determined by flow visualization by means of the oil–lampblack technique [15]. To facilitate the flow visualization, the surface of the cylinder was first covered with white, plasticized, self-adhering contact paper. The upstream edge of the contact paper was positioned about 0.6 cm downstream of the forward edge of the cylinder in order that the presence of the covering not affect the separation of the flow, which occurred at the forward edge. The covering extended well downstream of the reattachment station.

In preparation for a visualization run, a thin film of engine oil was applied to the contact paper. Then, a circular toothpick with a conical tip was dipped into a container filled with a mixture of oil and lampblack powder, and an array of small dots of the oil–lampblack solution was deployed axially along the topmost horizontal line of the cylinder. The dots were about 0.5 mm in diameter, and the distance between the centers of consecutive dots was 1.5 mm. The presence of the aforementioned thin film of oil enabled the dots to move readily even when subjected to very small airflow-induced shear stresses.

When the dots were in place, the airflow was initiated. It was soon observed that all dots upstream of a certain station moved in the direction opposite to the freestream, while all dots downstream of that station moved in the direction of the freestream. The demarcation between the upstream- and downstream-moving dots corresponds to the point of reattachment x_r. It was evaluated at the midpoint between the adjacent upstream- and downstream-moving dots. Consequently, the uncertainty in x_r is about $0.02D$ where D is the outer diameter of the cylinder.

The aforementioned visualization runs were performed for all the Reynolds numbers at which heat transfer data were collected and for each of the configurations pictured in Figs. 1(a)–(c). Note that the visualization runs were carried out separately from the heat transfer data runs.

Visualization runs were also performed to investigate the circumferential uniformity of the reattachment point. To this end, arrays of dots were placed along several axial lines distributed around the circumference. These runs affirmed that circumferential uniformity prevailed within the experimenter's capability to match the axial positions of the dots on the various axial lines. It was estimated that axial misalignments of about 1 mm occurred, yielding an uncertainty in the circumferential uniformity of about $0.02D$.

DATA REDUCTION AND NUMERICAL SOLUTIONS

Data reduction

The local heat transfer coefficient and Nusselt number at each of the measurement stations on the outer surface of the longitudinal cylinder were determined from the definitions

$$h = q/(T_w - T_\infty), \quad Nu = hD/k. \tag{1}$$

In the equation for h, T_w and T_∞ denote the local surface temperature and the freestream temperature, respectively, while q is the local convective heat flux from the surface to the airflow. To evaluate q, the power input to the stainless steel sheet as a whole was first prorated and then corrections were made for the local heat losses by radiation and conduction at the exposed and rear faces of the sheet, respectively. The prorating was validated by the measured linearity of the voltage along the cylinder.

The radiation corrections were obtained from the relation

$$\varepsilon\sigma(T_w^4 - T_\infty^4) \tag{2}$$

with $\varepsilon = 0.10$. Note that the temperature of the radiation environment was assumed equal to the freestream temperature T_∞. The conduction correction was the end result of a two-dimensional, axisymmetric, finite-difference computation which encompassed a solution domain consisting of the phenolic backing tube and the insulation-filled annular space adjacent to the backing tube. The details of the numerical work are set forth in ref. [14].

With regard to T_w, circumferential uniformity was achieved to within $\pm 1\%$ of $(T_w - T_\infty)$ or better. The two thermocouples for T_∞ yielded identical readings to within the ± 1 μV resolving power of the instrumentation.

The outer diameter D was used as the characteristic dimension in the Nusselt number, and the thermal conductivity k was evaluated at the freestream temperature. Since both D and k were constants for a given data run, the axial distribution of the Nusselt number is a direct reflection of the axial variation of the heat transfer coefficient.

The Reynolds number was expressed in the form

$$Re = U_\infty D/\nu \tag{3}$$

where, again, the cylinder diameter was used as the characteristic dimension. No blockage correction was needed in the determination of U_∞ since the frontal area of the cylinder was less than 1% of the cross-sectional area of the wind tunnel. The kinematic viscosity appearing in the Reynolds number was evalu-

ated at T_∞ and at the wind tunnel static pressure. Variable properties were not a significant factor since $(T_w - T_\infty) \sim 5°C$.

Numerical solutions

As was noted in the Introduction, numerical finite-difference solutions were performed for the blunt-face longitudinal cylinder (Fig. 1(a)) and for an abrupt enlargement in a parallel-plate channel (Fig. 1(d)). The solutions for both of these cases were for laminar, constant-property, non-buoyant flows with negligible viscous dissipation and compression work. The cylinder problem was solved in x, r axisymmetric cylindrical coordinates, while the channel solutions were performed in x, y Cartesian coordinates. For both cases, the fully elliptic forms of the conservation equations for mass, momentum, and energy were used, and no boundary-layer-type approximations were made.

For reasons having more to do with timing, personnel, and finance than with logic, different computational resources were employed in solving the aforementioned problems. For the longitudinal cylinder, a general-purpose computer program involving the SIMPLER algorithm of Patankar [16] was utilized in conjunction with a Cray 1 computer. That algorithm is based on physical variables (velocities, pressure, temperature). The abrupt enlargement problem was solved using a specifically written computer program [17] based on streamfunction–vorticity variables, plus temperature, with execution primarily on an IBM PC equipped with a math coprocessor.

The details of the numerical aspects of the solutions are well documented elsewhere and need not be repeated since the physical content of the final results is of main interest here. However, a moderate amount of background information is appropriate.

Longitudinal cylinder

In an earlier work [18], the authors dealt with a somewhat different version of the present blunt-faced, longitudinal cylinder problem. In particular, in response to experimental data available at that time, numerical solutions were obtained for the case in which the forward face of the cylinder was maintained at a uniform temperature different from that of the freestream, while the cylindrical surface was adiabatic. Nusselt numbers were obtained at the forward face for comparison with the experimental data. The solutions were for Reynolds numbers of 5000 and greater, further reflecting the operating conditions of the experiments. To ensure the accuracy of the numerical results, a careful study was performed in ref. [18] to optimize the placement of the boundaries of the solution domain, the number of grid points, and the grid deployment.

The thermal boundary conditions of interest here, uniform heat flux on the cylindrical surface and adiabatic on the forward face, are different from those of ref. [18]. For these boundary conditions, a solution was carried out for a Reynolds number $U_\infty D/\nu = 2000$ and a Prandtl number of 0.713. The selection of a Reynolds number lower than those of ref. [18] and of the present experiments was made to increase the likelihood that the assumption of laminar flow along the cylindrical surface would be valid.

The solution domain was set up with an upstream boundary 4.7 cylinder diameters ahead of the forward face, a downstream boundary 2.4 diameters from the forward face, and a cylindrical boundary 3.7 diameters from the cylinder axis. A 50×50 grid (axial $\times$ radial) was used. The grid deployment was accomplished in two steps. First, a tentative grid distribution was generated by use of a power-law function such that more grid points were packed in the vicinity of the solid surface, where the highest gradients were expected. Then, the results obtained using the tentative grid were graphed, and the grid points close to the solid boundaries were manually redeployed to better resolve the gradients.

From the solution, the axial distribution of the local heat transfer coefficient and Nusselt number at the outer surface of the cylinder were evaluated according to the definitions of equation (1), from which the location x_{max} of the maximum was determined. In addition, the streamwise velocity at the surface-adjacent grid point ($r/R = 1.00005$) at each axial station was plotted as a function of the axial coordinate. A change of sign of this velocity is tantamount to a change of sign of the wall shear stress. The location at which the sign change occurred was identified as the reattachment point x_r.

Abrupt enlargement

The numerical solutions to be reported here for the abrupt enlargement problem correspond to the ratio H_2/H_1 of the post-enlargement channel height to the pre-enlargement channel height equal to 2 (see Fig. 1(d) for the nomenclature). The section of channel which delivers the flow to the enlargement is sufficiently long to enable complete hydrodynamic development to occur, resulting in the attainment of a parabolic velocity profile. However, owing to the possible upstream propagation of fluid flow events associated with the enlargement, the parabolic velocity was imposed at $x = -H_1$ rather than at $x = 0$. The downstream end of the computational domain was placed at $x = 18z$, where the step height $z = (H_2 - H_1)$.

For the enlargement problem, the imposed thermal boundary conditions are uniform temperature T_w on the lower wall of the enlarged channel with all other bounding surfaces adiabatic (including the step). The fluid is delivered to the enlargement at a uniform temperature $T = T_1$, and this condition was applied at $x = -H_1$ instead of at $x = 0$ to accommodate possible upstream axial conduction.

As noted earlier, the numerical solutions were obtained by means of a special purpose computer program. The governing differential equations, their discretization, and the development of the computer

program are set forth in painstaking detail in ref. [17], with a listing of the program being provided in Appendix F. The ADI (alternating-direction implicit) method was used to solve the discretized equations in conjunction with the Thomas algorithm. Underrelaxation was incorporated to stabilize the iterative procedure. The solution domain was spanned by a non-uniform 77×77 (axial $\times$ transverse) grid whose layout is documented in Appendix E of ref. [17]. About 2000 iterations were required to converge the velocity solution. With the converged velocity field as input, the temperature solution converged in about 200 iterations.

The numerical solutions yielded the distribution of the local heat flux q along the lower wall of the enlarged channel as well as the fluid bulk temperature T_b at each axial station. The latter was evaluated from

$$T_b = \int_0^{H_2} Tu\,dy \Big/ \int_0^{H_2} u\,dy \tag{4}$$

where u is the streamwise velocity and y is the transverse coordinate. Note that due to the flow separation which occurs downstream of the enlargement step, u may be negative in some part of the cross-section.

Two pairs of heat transfer coefficients and Nusselt numbers were evaluated from the aforementioned information, namely

$$h = q/(T_w - T_b), \quad Nu = hz/k \tag{5}$$

and

$$h_1 = q/(T_w - T_1), \quad Nu_1 = h_1 z/k \tag{6}$$

where the step height z is used as the characteristic dimension. Whereas hz/k is a true dimensionless local heat transfer coefficient, $h_1 z/k$ is actually a dimensionless local heat flux. The two quantities were evaluated in order to compare the locations x_{max} at which their axial distributions attained maxima.

To determine the reattachment point x_r, the wall-adjacent streamwise velocity at each axial station was evaluated from the streamfunction at the grid point nearest to the lower wall of the enlarged channel. These velocities correspond to a distance $y = 0.00226z$ from the wall. Their axial distribution was characterized by a change of sign, which corresponds to x_r.

The Reynolds number for the abrupt enlargement problem was defined as

$$Re = \bar{u}_1 z/\nu \tag{7}$$

in which $\bar{u}_1$ is the mean velocity in the pre-enlargement portion of the channel, and the step height z is the characteristic dimension. The solutions were performed for Reynolds numbers of 100, 200, and 300 and for a Prandtl number of 0.7.

RESULTS AND DISCUSSION

Experimental results

Representative results for the axial distribution of the local Nusselt number on the outer surface of the longitudinal cylinder are presented in Fig. 2. Although the figure is specific to the blunt-face case, the qualitative trends are also applicable to the open and cavity cases, for which results are available in ref. [19].

In Fig. 2, the local Nusselt number hD/k is plotted as a function of the dimensionless axial coordinate x/D for parametric values of the Reynolds number ranging from about 7700 to 47,000. For all of the Reynolds numbers, the axial distributions have a common shape characterized by an initial increase, a local maximum, and subsequent monotonic decrease. It is seen that x_{max}, the location of the Nusselt number maximum, is on the order of one cylinder diameter. It is also evident that, overall, x_{max} increases as the Reynolds number increases.

From enlarged versions of Fig. 2 and corresponding figures for the open and cavity configurations, values of x_{max} for each Reynolds number were determined by graphical interpolation. These results, recast as x_{max}/D, are plotted as a function of the Reynolds number in Figs. 3–5 along with the reattachment point locations x_r/D obtained from the flow visualization experiments. Figure 3 conveys results for the blunt-face case, Fig. 4 for the open-bore case, and Fig. 5 for the cavity case. In each of these figures, x_{max}/D and x_r/D are represented by circular and square data symbols, respectively.

An overall inspection of Figs. 3–5 indicates that for all three investigated fluid flow configurations, the

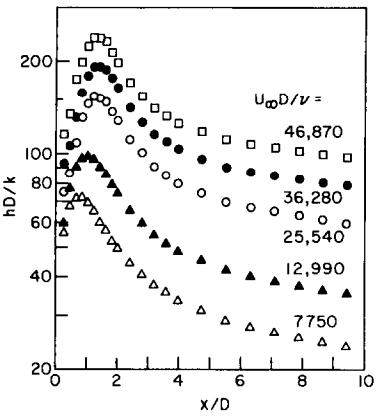

FIG. 2. Axial distributions of the local Nusselt number for the blunt-face longitudinal cylinder.

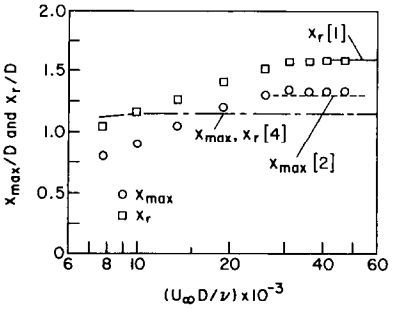

FIG. 3. Values of x_{max} and x_r for the blunt-face longitudinal cylinder.

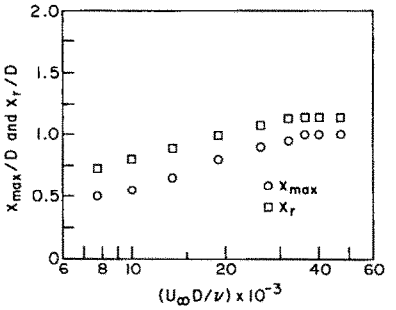

FIG. 4. Values of x_{max} and x_r for the open-bore longitudinal cylinder.

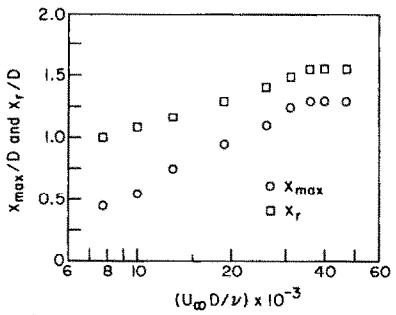

FIG. 5. Values of x_{max} and x_r for the longitudinal cylinder with a forward-facing cavity.

Nusselt number maximum occurs upstream of the reattachment point. That is, the location of the maximum lies within the separation bubble. For the most part, x_{max} is about a quarter of a diameter smaller than x_r, but the deviation is greater (about a half diameter) for the cavity case at low Reynolds numbers. Thus, the results of Figs. 3–5 provide conclusive evidence that the common assumption of $x_{max} = x_r$ is, at best, a special case. A discussion of various factors which affect the relationship between x_{max} and x_r will be deferred until the end of the paper.

The trend of the results with Reynolds number is the same for x_{max} and x_r for all three investigated configurations. For Reynolds numbers up to about 30,000, x_{max} and x_r increase with increasing Reynolds number but then become invariant with further increases in the Reynolds number. This invariance suggests that the separated region may have become turbulent. The Reynolds-number-related increase in x_{max} and x_r is about half a diameter for five of the six cases depicted in Figs. 3–5, while for the sixth case (x_{max} for the cavity), the increase is even larger. The consistency of the trend with Reynolds number among the investigated cases casts some doubt on prior low-Reynolds-number results which showed x_{max} and/or x_r to be independent of the Reynolds number.

The x_{max} and x_r values for the blunt-face case are substantially larger (by about $0.35D$) than those for the open-bore case (compare Figs. 3 and 4). This finding is physically plausible. For the blunt-face case, the vigor of the radial outflow along the forward face of the cylinder is necessarily greater than that for the open-bore case. The stronger the radial outflow, the thicker and longer is the separation bubble, which leads to larger x_{max} and x_r. For the cavity case, the x_{max} and x_r values are, for the most part, not very different from those for the blunt-face case, which is physically reasonable; significant differences occur only for x_{max} at the lower Reynolds numbers.

Attention is now turned to a comparison of the present results for the blunt-face case with those of the literature. References [1, 2] were companion studies which covered different Reynolds number ranges and which overlap the present Reynolds number range only at its high end. Within the range of overlap, excellent agreement prevails for both x_{max} and x_r, as can be seen from Fig. 3. In ref. [4], no distinction was made between x_{max} and x_r and, apparently, virtually no effect of the Reynolds number on these quantities was encountered. The deviations in evidence in Fig. 3 between the present results and those of ref. [4] may well be due to differences in freestream turbulence level in the two investigations (0.9–1.4% in ref. [4] vs 0.4–0.5% for the present).

Numerical results

The numerically determined axial distributions of the local Nusselt number and of the wall-adjacent streamwise velocity at the outer surface of the blunt-face cylinder are presented in Fig. 6. These results are for laminar flow and for Reynolds and Prandtl numbers of 2000 and 0.713, respectively.

The Nusselt number distribution of Fig. 6 exhibits the same qualitative trends as the experimentally determined distributions of Fig. 2 (note that the enlarged abscissa scale of Fig. 6 flattens the maximum). The velocity adjacent to the surface of the cylinder is negative for $x/D < 1.17$ and becomes positive thereafter. The negative velocities correspond to the backflow leg of a recirculation loop. Since the wall shear stress is proportional to the surface-adjacent velocity, it follows that the shear changes sign at $x/D = 1.17$, signaling the reattachment of the flow. Consequently, the separation bubble extends from $x/D = 0$ to 1.17.

From Fig. 6, x_{max}/D can be read as 0.82, while $x_r/D = 1.17$. Thus, as in the experiments, the Nusselt number attains its maximum in the separated region, upstream of the point of reattachment of the flow. The spread between these values of x_{max}/D and x_r/D is similar to that of the experiments. However, the actual magnitudes of x_{max}/D and x_r/D are moderately different from those obtained by extrapolating the data of Fig. 2. These deviations are undoubtedly due to the laminar flow model.

Within the separated region, the magnitude of the wall-adjacent velocity increases at first, attains a maximum, and then decreases toward zero. The maximum occurs where the ellipse-like streamlines which characterize the recirculating flow in the separation bubble approach most closely to the cylinder surface. Note that the Nusselt number maximum is

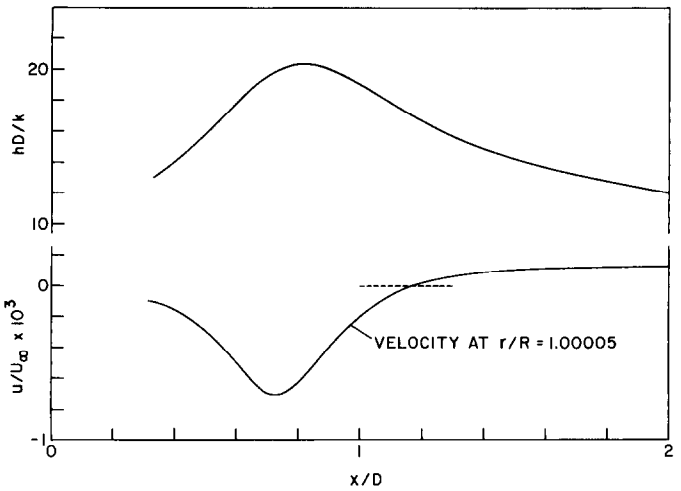

FIG. 6. Numerically determined axial distributions of the local Nusselt number and the wall-adjacent streamwise velocity for the blunt-face longitudinal cylinder, $U_\infty D/\nu = 2000$.

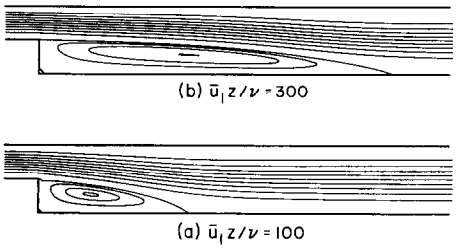

FIG. 7. Streamline patterns for the case of an abrupt enlargement in a parallel-plate channel.

attained quite close to the location where the velocity magnitude attains its maximum.

Attention is next turned to the results for the abrupt enlargement which, as noted earlier, also correspond to laminar flow. The streamline patterns for Reynolds numbers $\bar{u}_1 z/\nu$ of 100 and 300 are illustrated in Fig. 7 (the results for $\bar{u}_1 z/\nu = 200$ are omitted due to space limitations). As seen in the figure, the length of the separation bubble is strongly affected by the Reynolds number, with greater elongation occurring as the Reynolds number increases. The streamline which cordons off the separation bubble (i.e. the dividing streamline) bounds a recirculation zone within which the streamlines are ellipse-like in form.

Further inspection of the recirculation streamlines indicates that the wall-adjacent flow in the downstream portion of the separation bubble has a component of velocity directed toward the wall. A wall-directed flow also occurs downstream of the bubble. In contrast, in the upstream portion of the bubble, there is a component of velocity directed away from the lower wall. It is reasonable to expect that the direction of the flow either toward or away from the wall would affect the value of the heat transfer coefficient as would, of course, the magnitude of the streamwise velocity adjacent to the wall.

Axial distributions of the local Nusselt number, dimensionless wall heat flux, and wall-adjacent velocity along the lower wall of the enlarged portion of the channel are presented in Figs. 8 and 9 for Reynolds numbers $\bar{u}_1 z/\nu$ of 100 and 300. The two heat-transfer-related curves in each figure display their expected maxima, with x_{max} for the Nusselt number distribution lying slightly downstream of the x_{max} for the heat flux distribution. Also, as expected, the values of hz/k

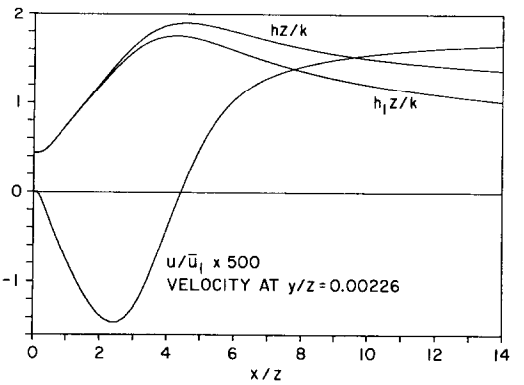

FIG. 8. Axial distributions of the local Nusselt number, dimensionless wall heat flux, and wall-adjacent streamwise velocity for the abrupt enlargement case, $\bar{u}_1 z/\nu = 100$.

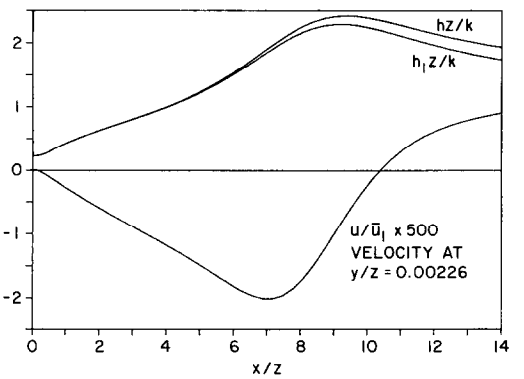

FIG. 9. Axial distributions of the local Nusselt number, dimensionless wall heat flux, and wall-adjacent streamwise velocity for the abrupt enlargement case, $\bar{u}_1 z/\nu = 300$.

Table 1. Values of x_{max} and x_r for abrupt enlargement

		x_{max}/z for	
$\bar{u}_1 z/\nu$	x_r/z	hz/k	$h_1 z/k$
100	4.405	4.533	4.218
200	7.672	7.167	6.909
300	10.380	9.431	9.222

exceed the values of $h_1 z/k$ since $(T_w - T_b)$ is smaller than $(T_w - T_1)$. The distribution of the wall-adjacent velocity also displays a maximum in its magnitude. The various maxima and the point where the velocity changes sign are shifted downstream as the Reynolds number increases.

The values of x_{max} and x_r for the abrupt enlargement are listed in Table 1. As seen there, the x_{max} values for the lowest Reynolds number straddle x_r, while for the higher Reynolds numbers x_{max} is smaller than x_r. The aforementioned difference in the relationship between x_{max} and x_r (i.e. greater or smaller) is believed related to the aspect ratio of the separation bubble. For relatively long bubbles, $x_{max} < x_r$, while for relatively short bubbles, $x_{max} > x_r$. The separation bubbles for the longitudinal cylinder fall into the longer category, which is consistent with the finding that $x_{max} < x_r$.

CONCLUDING REMARKS

The results obtained here, both experimental and numerical, have provided conclusive evidence that the common assumption of $x_{max} = x_r$ is, at best, a special case. Two factors affecting the relationship between x_{max} and x_r, not previously identified in the literature, are the magnitude of the wall-adjacent streamwise velocity (in particular, the velocity maximum) and the direction of the transverse velocity in the wall-adjacent flow. For relatively long separation bubbles, it is believed that the former is the major factor in causing $x_{max} < x_r$. On the other hand, for relatively short separation bubbles, the wall-directed transverse velocity in the neighborhood and downstream of the reattachment point leads to $x_{max} > x_r$.

REFERENCES

1. T. Ota, An axisymmetric separated and reattached flow on a longitudinal blunt circular cylinder, *J. appl. Mech.* **42,** 311–315 (1975).
2. T. Ota and N. Kon, Heat transfer in an axisymmetric separated and reattached flow over a longitudinal blunt circular cylinder, *J. Heat Transfer* **99,** 155–157 (1977).
3. V. Kottke, H. Blenke and K. G. Schmidt, Determination of the local and average mass transfer on thick plates in parallel flow with flow separation and reattachment, *Wärme- u. Stoffübertr.* **10,** 217–232 (1977).
4. V. Kottke, H. Blenke and K. G. Schmidt, The influence of nose section and turbulence intensity on the flow around thick plates in parallel flow, *Wärme- u. Stoffübertr.* **10,** 159–174 (1977).
5. T. Ota and N. Kon, Heat transfer in the separated and reattached flow on a blunt flat plate, *J. Heat Transfer* **96,** 459–462 (1974).
6. T. Ota and M. Itaska, A separated and reattached flow on a blunt flat plate, *J. Fluids Engng* **98,** 79–86 (1976).
7. T. Ota and N. Kon, Heat transfer in the separated and reattached flow over blunt flat plates—effects of nose shape, *Int. J. Heat Mass Transfer* **22,** 197–206 (1979).
8. D. C. McCormick, R. C. Lessmann and F. L. Test, Heat transfer to separated flow regions from a rectangular prism in a cross stream, *J. Heat Transfer* **106,** 276–283 (1984).
9. W. Aung, An experimental study of laminar heat transfer downstream of back steps, *J. Heat Transfer* **105,** 823–829 (1983).
10. R. A. Seban, A. Emery and A. Levy, Heat transfer to separated and reattached subsonic turbulent flows obtained downstream of a surface step, *J. Aerospace. Sci.* **26,** 809–814 (1959).
11. J. C. Vogel and J. K. Eaton, Combined heat transfer and fluid dynamic measurements downstream of a backward-facing step, *J. Heat Transfer* **107,** 922–929 (1985).
12. W. H. Emerson, Heat transfer in a duct in regions of separated flow, *Proc. 3rd Int. Heat Transfer Conf.*, Vol. II, pp. 267–275 (1966).
13. Y. Kang, J. Nishino, K. Suzuki and T. Sato, Application of flow and surface temperature visualization techniques to a study of heat transfer in recirculating flow regions. In *Flow Visualization II* (Edited by W. Merzkirch), pp. 77–81. Hemisphere, Washington, D.C. (1982).
14. S. S. Kang, Heat transfer from a hollow-bore circular cylinder situated longitudinal to a freestream flow, Ph.D. thesis, Department of Mechanical Engineering, University of Minnesota, Minneapolis, Minnesota (1985).
15. W. Merzkirch, *Flow Visualization.* Academic Press, New York (1974).
16. S. V. Patankar, *Numerical Heat Transfer and Fluid Flow.* Hemisphere, Washington, D.C. (1980).
17. W. Chuck, Evaporation of water from a recessed surface to a parallel forced convection airflow, Ph.D. thesis, Department of Mechanical Engineering, University of Minnesota, Minneapolis, Minnesota (1985).
18. S. S. Kang and E. M. Sparrow, Heat and mass transfer at an upstream-facing blunt face situated in a uniform oncoming flow, *Numer. Heat Transfer* **9,** 419–439 (1986).
19. S. S. Kang and E. M. Sparrow, Heat transfer from an open- or closed-bore cylinder situated longitudinal to a freestream, *J. Heat Transfer* (1987), in press.

RELATION ENTRE LE POINT DE RECOLLEMENT D'ECOULEMENT ET LE MAXIMUM DE TRANSFERT THERMIQUE POUR DES REGIONS DE SEPARATION D'ECOULEMENT

Résumé—La distribution du nombre de Nusselt dans et juste après une région de séparation d'écoulement montre l'existence d'un maximum situé au point de réattachement de l'écoulement. Des expériences en soufflerie concernent un cylindre circulaire orienté longitudinalement à un écoulement libre. A cause du décollement d'écoulement au pourtour de la face avant du cylindre, la portion en aval de la surface du cylindre est balayée par une zone de recirculation du fluide. Trois configurations du cylindre sont étudiées : une avec une face avant arrondie, une autre avec un trou ouvert reliant les deux extrémités et une dernière pour laquelle le trou est fermé à l'extrémité arrière. On résout numériquement le premier cas. Des solutions numériques additionnelles sont apportées pour le cas d'un brusque élargissement dans un canal entre plans parallèles. Les résultats expérimentaux et théoriques montrent ensemble que l'hypothèse courante d'une coïncidence des points de recollement d'écoulement et de maximum de coefficient de transfert est, au mieux, un cas particulier. Dans la plupart des cas étudiés, le maximum de transfert se produit en aval du point de recollement. On identifie les facteurs qui agissent sur les positions respectives du maximum et du recollement.

ZUSAMMENHANG ZWISCHEN DEM WIEDERANLEGEN DER STRÖMUNG UND DEM MAXIMALEN WÄRMEÜBERGANG FÜR ABLÖSEZONEN

Zusammenfassung—Die Verteilung der Nusselt-Zahl in Strömungsrichtung in einer Ablösezone und unmittelbar dahinter zeigt ein Maximum, dessen Lage—relativ zum Ort des Wiederanlegens der Strömung—in dieser Arbeit untersucht wurde. Es wurden Windkanalexperimente durchgeführt, bei denen Kreiszylinder längs eines gleichmäßigen Freistrahls angeordnet wurden. Infolge von Grenzschichtablösung am äußeren Rand der Stirnseite des Zylinders wurden die stromaufwärtsliegenden Bereiche der Zylindermantelfläche von rezirkulierendem Fluid umspült. Es wurden drei Ausführungen des Zylinders untersucht: einer mit einer stumpfen Stirnseite, ein zweiter mit Bohrungen an den stromaufwärts bzw. stromabwärts gerichteten Stirnseiten und ein dritter mit verschlossener Bohrung am stromabwärtsgerichteten Ende. Die Anordnung mit stumpfer Stirnfläche wurde zusätzlich numerisch untersucht. Zusätzliche numerische Lösungen konnten für den völlig anders gearteten Fall einer plötzlichen Erweiterung in einen Kanal aus parallelen Platten gewonnen werden. Sowohl Experiment als auch die numerischen Ergebnisse lieferten schlüssige Aussagen darüber, daß die im allgemeinen angenommene Identität von Strömungswiederanlegungspunkt und maximalem Wärmeübergangskoeffizient bestenfalls als Spezialfall aufrecht erhalten werden kann. Für die überwiegende Anzahl der hier untersuchten Fälle liegt das Maximum des Wärmeübergangs stromaufwärts vom Strömungswiederanlegungspunkt. Es wurden die Größen bestimmt, die die relative Lage beider Orte beeinflussen.

СООТНОШЕНИЯ МЕЖДУ ПОЛОЖЕНИЕМ ТОЧКИ ПРИСОЕДИНЕНИЯ ПОТОКА И МАКСИМУМОМ ТЕПЛООТДАЧИ ДЛЯ ЗОНЫ ОТРЫВНЫХ ТЕЧЕНИЙ

Аннотация—Распределение числа Нуссельта по направлению потока в пределах зоны отрыва течения и непосредственно за ней имеет максимум, положение которого относительно точки присоединения потока исследовано в данной работе. Проведены эксперименты в аэродинамической трубе, в которой круговой цилиндр ориентировался вдоль однородного свободного потока. Из-за отрыва потока на передней кромке торца цилиндра начальная часть боковой поверхности цилиндра омывалась зоной рециркулирующей жидкости. Исследовались три конфигурации цилиндра: один с твердым затупленным передним торцом, другой—с полым внутренним каналом, открытым с обоих концов, третий—с заглушенным сзади полым внутренним каналом. Случай затупленного переднего торца исследовался также численно. Дополнительные численные решения получены для отличного от рассмотренных случая плоскопараллельного канала с внезапным расширением. Экспериментальные и теоретические результаты убедительно доказали, что общепринятое предположение о совпадении точки присоединения потока и максимума коэффициента теплообмена является случайным. Для большинства исследуемых примеров максимум теплообмена находится выше по течению от точки присоединения. Определены факторы, влияющие на относительное положение максимума и точки присоединения.